Evidence of radical chemistry in catalytic methane oxybromination

Vladimir Paunović[1], Patrick Hemberger[2], Andras Bodi[2], Núria López[3] and Javier Pérez-Ramírez[1]*

Unravelling the pathways of catalytic methane functionalization sets the foundations for the efficient production of valuable chemicals and fuels from this abundant feedstock. The catalytic oxybromination of methane into platform compounds bromomethane and dibromomethane constitutes a prominent example, although it displays a puzzling reaction network that has been speculated to involve free-radical intermediates. Here, photoelectron photoion coincidence spectroscopy with synchrotron radiation was used to provide evidence of the evolution of gaseous methyl and bromine radicals over $(VO)_2P_2O_7$ and EuOBr catalysts and the strong correlation between the formation of methyl radicals and the production of bromomethanes. Complemented by kinetic data on methane oxybromination and non-catalytic methane bromination, these results imply the surface-catalysed generation of bromine radicals and molecular bromine followed by the gas-phase methane bromination, which is rationalized by density functional theory calculations. The findings emphasize the role of both surface and gas-phase steps in halogen-mediated C–H bond activation over heterogeneous catalysts.

Understanding the mechanisms of the heterogeneously catalysed functionalization of methane (CH_4) and other light alkanes contained in natural gas goes well beyond a scientific curiosity, as it may unlock the transformation of this increasingly abundant, relatively cheap and potentially renewable feedstock into commodities[1–10]. This challenging task requires sophisticated kinetic, spectroscopic and theoretical approaches to uncover the reaction pathways, their elementary steps and the underlying reactive intermediates, with the ultimate aim of translating this information into the design of selective catalytic processes[1–12]. Particularly complex cases include processes such as oxidative coupling[1,6,11,12], oxidative dehydrogenation[2,4], selective oxidation into alcohols and aldehydes[13], transformation into olefins and aromatics[3] or the reaction of CH_4 with ammonia[14], wherein the species formed on the catalyst surface might enter gas-phase reactions leading to desired and undesired products. A mechanism involving interplay between surface-catalysed and gas-phase reaction steps has been hypothesized for the catalytic oxybromination of methane (equations (1) and (2)) into bromomethanes, methyl bromide (CH_3Br) and dibromomethane (CH_2Br_2), which represent attractive platform compounds for the manufacture of chemicals and fuels[15–19].

$$CH_4 + HBr + \frac{1}{2}O_2 \rightarrow CH_3Br + H_2O \quad (1)$$

$$CH_4 + 2HBr + O_2 \rightarrow CH_2Br_2 + 2H_2O \quad (2)$$

$$CH_4 + Br_2 \rightarrow CH_3Br + HBr \quad (3)$$

$$CH_4 + 2Br_2 \rightarrow CH_2Br_2 + 2HBr \quad (4)$$

$$2HBr + \frac{1}{2}O_2 \rightarrow Br_2 + H_2O \quad (5)$$

Among the catalytic materials reported, vanadyl pyrophosphate ($(VO)_2P_2O_7$, VPO) and europium oxybromide (EuOBr) provided the highest selectivity to CH_3Br and CH_2Br_2 with minimal production of undesired carbon oxides (CO_x)[16,17]. Steady-state reaction tests over multiple catalysts pointed out that methane oxybromination commonly occurs at similar temperatures (≥693 K) to the non-catalysed gas-phase bromination (equations (3) and (4)). Moreover, an increase in the production of bromomethanes in oxybromination was coupled with a drop in bromine (Br_2) evolution, which is the main reaction product at low temperatures[16,17,20]. This led to the proposal that the reaction mechanism may synergistically involve the surface-catalysed oxidation of hydrogen bromide (HBr, equation (5)) into Br_2 and methane bromination in the gas phase (equations (3) and (4))[16], which proceeds via methyl ($CH_3^{\bullet}$) and bromine ($Br^{\bullet}$) radicals[21–23]. However, this reaction pathway has not yet been demonstrated experimentally. In this sense, a theoretical study on lanthanum oxide surfaces suggested that the adsorption of HBr or Br_2 in the presence of oxygen (O_2) might facilitate the surface-catalysed activation of the C–H bond[24]. Hence, to unequivocally unravel the mechanism of methane oxybromination requires the detection of radical intermediates during the reaction (under operando conditions), which is highly challenging given their short lifetimes and the extremely corrosive reaction environment.

Lunsford and co-workers pioneered the application of matrix isolation electron spin resonance spectroscopy (MIESR) to confirm the formation of alkyl radicals in catalytic processes such as oxidative coupling of methane and *n*-propene oxidation[11,25]. More recently, molecular beam mass spectrometry (MS) coupled with electron impact ionization (EI) was used to directly detect short-lived gaseous intermediates in the synthesis of hydrogen cyanide from CH_4 and ammonia over a platinum catalyst[14]. However, the use of a high ionization energy (approximately 70 eV) leads to significant fragmentation of molecular ions and limits the application of EI. In contrast, the photoionization of molecular beam by vacuum ultraviolet (VUV) synchrotron radiation enables the photon energy

[1]Institute for Chemical and Bioengineering, Department of Chemistry and Applied Biosciences, ETH Zurich, Zurich, Switzerland. [2]Laboratory for Synchrotron Radiation and Femtochemistry, Paul Scherrer Institute, Villigen, Switzerland. [3]Institute of Chemical Research of Catalonia (ICIQ), Barcelona Institute of Science and Technology, Tarragona, Spain. *e-mail: jpr@chem.ethz.ch

to be fine-tuned, which suppresses the fragmentation interferences and boosts the sensitivity[12,26]. VUV photoionization mass spectroscopy (VUV-PIMS) was successfully applied to trace transient gaseous intermediates formed in combustion[26] and heterogeneously catalysed reactions such as the activation of CH_4[3,12], oxidation of volatile organics[27] and conversion of syngas[28]. Further advances have been achieved through the development of VUV photoelectron photoion coincidence (PEPICO) spectroscopy based on mass analysis of photoions and kinetic energy analysis of photoelectrons in delayed coincidence, which in combination with the high energy resolution, high dynamic range and fragment-free ionization, offers the possibility to measure photoion mass-selected (threshold) photoelectron spectra[29]. This makes it a powerful tool for an isomer-specific detection of short-lived species such as radicals in complex gas-phase reactions, as demonstrated by the studies on non-catalytic (bi)molecular rearrangements[30,31], flame chemistry[32] and catalytic pyrolysis of biomass[33]. Accordingly, PEPICO can be a decisive technique for interrogating the formation of gaseous intermediates in the heterogeneously catalysed halogen-based processes of C–H bond activation under operando conditions.

In the present work, we analyse the steady-state kinetic fingerprints of catalytic methane oxybromination over VPO and EuOBr (equations (1) and (2)) and non-catalytic gas-phase bromination (equations (3) and (4)), evidence for the importance of gas-phase chemistry in the former reaction (equations (1) and (2)). Operando PEPICO spectroscopic experiments demonstrate the formation of $CH_3^\bullet$ and $Br^\bullet$ radicals in the oxybromination chemistry and verify their crucial role in CH_4 activation. Density functional theory (DFT) strengthens the understanding of the surface and gas-phase processes at the molecular level.

Results

Evaluation of the reaction kinetics. Preliminary insights into the mechanism of methane oxybromination were gained by studying the steady-state kinetics over the best-performing EuOBr and VPO catalysts (Fig. 1), the structure of which was confirmed by X-ray diffraction analysis (Supplementary Fig. 2). The kinetic fingerprints were compared with those of the non-catalytic gas-phase bromination of methane (Fig. 1), as the latter reaction is known to proceed via homolytic scission of the C–H bonds by bromine radicals[21–23], which has been speculated as the pathway of CH_4 activation in catalytic oxybromination[16,17,20]. As shown in Fig. 1a (top), the temperature at which methane oxybromination is initiated (the light-off temperature) was very similar to that of methane bromination. An increased yield of bromomethanes (CH_3Br and CH_2Br_2) in oxybromination correlated with a drop in the Br_2 yield (Fig. 1a, top), which hints that the latter product might react with methane to generate the brominated hydrocarbons. Furthermore, the dependence of the selectivity to CH_3Br and CH_2Br_2 on the conversion of CH_4 in the oxybromination and the bromination followed a very similar trend (Fig. 1a, bottom), which was particularly evident in the case of highly selective EuOBr catalyst. The lower selectivity to bromomethanes over VPO is caused by its higher propensity to oxidize them to CO_x.

An additional link between the oxybromination and the bromination is inferred from the similarity of their kinetic parameters. The apparent reaction orders of the non-catalytic methane bromination with respect to CH_4 of approximately 1 and Br_2 of approximately 0.5 are consistent with its well-established radical-chain mechanism (Fig. 1b)[21–23]. The oxybromination displays relatively low positive orders with respect to HBr and O_2 of around 0.15–0.3, which suggest their fast activation, and the order of approximately 0.8 with respect to CH_4, which is comparable to that observed in methane bromination. The apparent activation energies of methane oxybromination over VPO (approximately 122 kJ mol^{-1}) and EuOBr (roughly 105 kJ mol^{-1}) catalysts also approach the value of this parameter in methane bromination (approximately 120 kJ mol^{-1}, Fig. 1c). In contrast, they are substantially different to the apparent activation barriers of methane oxidation (~64–72 kJ mol^{-1}, Fig. 1c), which is used as a probe reaction to determine the possibility of catalytic C–H bond scission. The oxidation yields CO and CO_2 as the only products, with no detectable partially oxidized intermediates, such as methanol (Supplementary Fig. 3). Notably, EuOBr and VPO are one order of magnitude less active in methane oxidation compared with oxybromination, which points to their low propensity to activate methane (vide infra). In accordance with this result, the enlargement of the void zone after the catalyst bed (post-catalyst volume), which provides additional time for the gaseous intermediates to react and is hence used to verify the occurrence of the gas-phase reaction steps[34], led to a progressive increase in the yield of bromomethanes and a decrease in the yield of Br_2 (Fig. 1d).

Detection of free radicals. The above-discussed kinetic fingerprints provide a strong hint that the mechanism of methane oxybromination probably involves the surface-catalysed HBr oxidation followed by the bromination of methane in the gas phase. Nonetheless, it could only be verified through a detection of the key gaseous intermediates participating in the homolytic mechanism of C–H bond splitting. Catalytic oxybromination of methane was therefore studied by depositing VPO and EuOBr catalysts on the walls of a tubular reactor placed in the source chamber of the PEPICO spectroscopy set-up (Fig. 2)[31], which comprises a powerful technique to selectively (by isomer) trace the formation of highly reactive gaseous species, such as radicals[29–33,35]. This reactor configuration and gas-phase sampling set-up minimized the quenching of the short-lived reaction intermediates that are desorbed from the catalyst surface or generated in the gas phase above the catalyst, by high dilution of the feed and low pressure inside the reactor (approximately 1–4 kPa) and the source chamber surrounding its outlet (roughly 2 mPa). The effluent reactor stream forms a molecular beam, which is skimmed and ionized by monochromatic VUV radiation, yielding photoelectrons and photoions that are detected in delayed coincidence[29,31]. In line with the steady-state catalytic tests, mass spectra of the outlet reactor feed recorded using different ionization energies provided evidence that besides the ions of respective reactants (CH_4 (m/z = 16), O_2 (m/z = 32) and HBr (m/z = 80/82)), the ions of the oxybromination products (CH_3Br (m/z = 94/96) and Br_2 (m/z = 158/160/162)) were also present (Fig. 3a, Supplementary Figs. 4,5). Ions of CH_3^+ (m/z = 15) and Br^+ (m/z = 79/81) could be unambiguously related to the ionization of the corresponding $CH_3^\bullet$ and $Br^\bullet$ radicals using photon energies of 10.0 eV and 13.6 eV, respectively (Fig. 3a, Supplementary Figs. 4,5). The photoionization energy at which the spectra of CH_3^+ were recorded sits well below the threshold for dissociative photoionization of CH_4 (14.3 eV) and CH_3Br (12.8 eV) that could potentially yield ions at m/z = 15 on VUV irradiation, corroborating the formation of CH_3^+ ions from $CH_3^\bullet$, which undergoes ionization at 9.84 eV[36–38]. This is confirmed by the photoion mass-selected threshold photoelectron spectra (ms-TPES), which show a peak at 9.84 eV (Fig. 3b) in accordance with the reported ionization energy of $CH_3^\bullet$[38]. In a similar manner to the detection of $CH_3^\bullet$, the VUV photon energy at which Br^+ ions were observed is below the dissociative photoionization threshold of HBr (15 eV), Br_2 (13.8 eV), CH_3Br (14.8 eV) and CH_2Br_2 (15.5 eV)[36,39,40]. Hence, the ions at m/z = 79/81 could only stem from the direct photoionization of $Br^\bullet$, which occurs at 11.8 eV[36]. Additional information can be gained by momentum imaging: as the gas sample leaves the reactor a molecular beam is formed that travels at almost the speed of sound and the gaseous species exhibit a narrow speed distribution (blue and red spots in Fig. 3c) perpendicular to the beam axis (that is, along x, Fig. 3c). In contrast, the ionized background gas features room-temperature velocities in both the x and y directions, which are imaged as an almost circular spot (yellow room-temperature

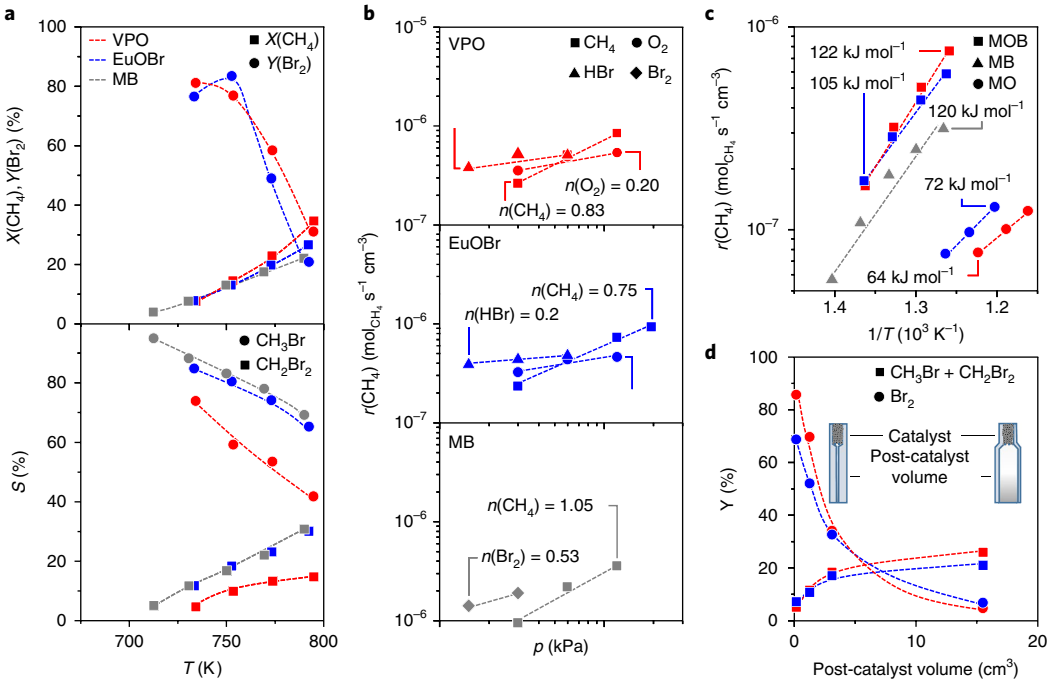

Fig. 1 | Kinetics of methane oxybromination, bromination and oxidation. **a**, The conversion of methane, yield of bromine (top) and selectivity to bromomethanes (bottom) versus temperature in methane oxybromination (CH_4:HBr:O_2:Ar:He = 6:6:3:4.5:80.5) over VPO and EuOBr catalysts, and in non-catalytic gas-phase methane bromination (MB, CH_4:Br_2:Ar:He = 6:3:4.5:86.5). **b**, The reaction rate versus the inlet partial pressure (p) of CH_4 (CH_4:HBr(Br_2):O_2:Ar:He = 3–20:6(3):3(0):4.5:83.5(86.5)–66.5(69.5)); HBr (CH_4:HBr:O_2:Ar:He = 6:3–12:3:4.5:83.5–74.5); O_2 (CH_4:HBr:O_2:Ar:He = 6:6:1.5–6:4.5:82–77.5); and Br_2 (CH_4:Br_2:Ar:He = 6:3–6:4.5:86.5–83.5) in methane oxybromination (T = 773 K) over VPO (top), EuOBr (middle) and non-catalytic gas-phase methane bromination (bottom, T = 753 K). **c**, Arrhenius plots of methane oxybromination (MOB) and methane oxidation (MO) over VPO (red) and EuOBr (blue) catalysts and for MB (grey). **d**, The yield of bromomethanes and bromine versus post-catalyst volume in methane oxybromination (CH_4:HBr:O_2:Ar:He = 6:6:3:4.5:80.5, T = 773 K) over VPO (red) and EuOBr (blue). The apparent activation energies and the partial reaction orders are stated in the respective plots in **b** and **c**. The catalytic oxybromination of methane was performed using W_{cat} = 1.0 g and V_{bed} = 2.0 cm^3 in the tests presented in **a**–**c**, and W_{cat} = 0.07 g, V_r = 0.1 cm^3 in **d**. The non-catalytic gas-phase bromination was studied using V_r = 3.1 cm^3. All of the tests were conducted using F_T = 100 cm^3 min^{-1} at total pressure (P) of 1 bar.

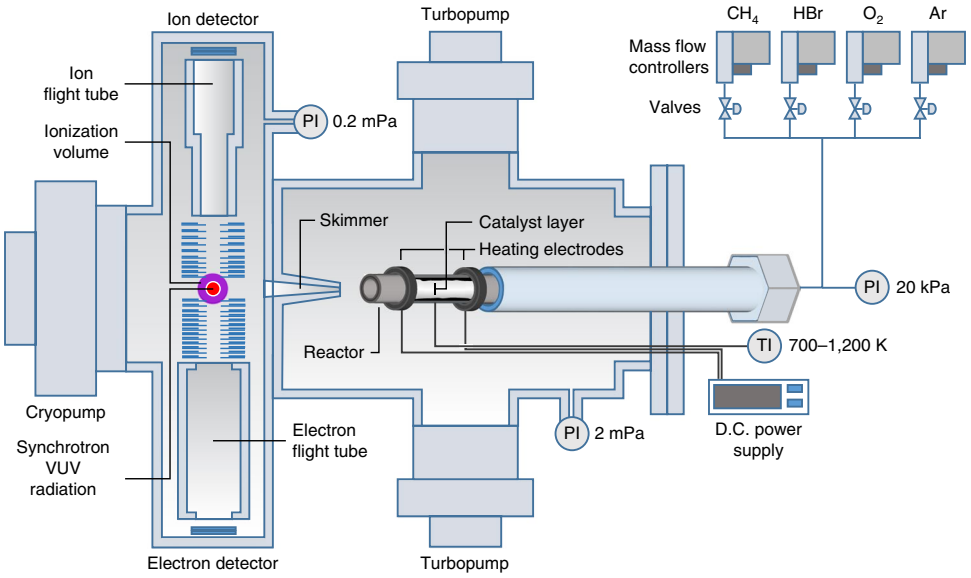

Fig. 2 | PEPICO reactor set-up for radical detection. The reaction mixture is fed by a set of digital mass-flow controllers to the SiC reactor of small diameter (1.0 mm) placed in the source chamber. The reactor has an oxybromination catalyst deposited on its inner walls and is heated resistively, with the temperature monitored by a thermocouple attached to its outside wall. The central part of the molecular beam escaping the reactor is selected by a skimmer and fed to the analysis chamber, wherein it is photoionized by monochromatic synchrotron radiation. Generated photoions and photoelectrons are accelerated in opposite directions by a constant electric field and the resulting velocity map imaged by the two delay-line anode detectors in delayed coincidence. TI and PI refer to temperature and pressure indicators, respectively. Further details on the set-up and operation are provided in the Methods.

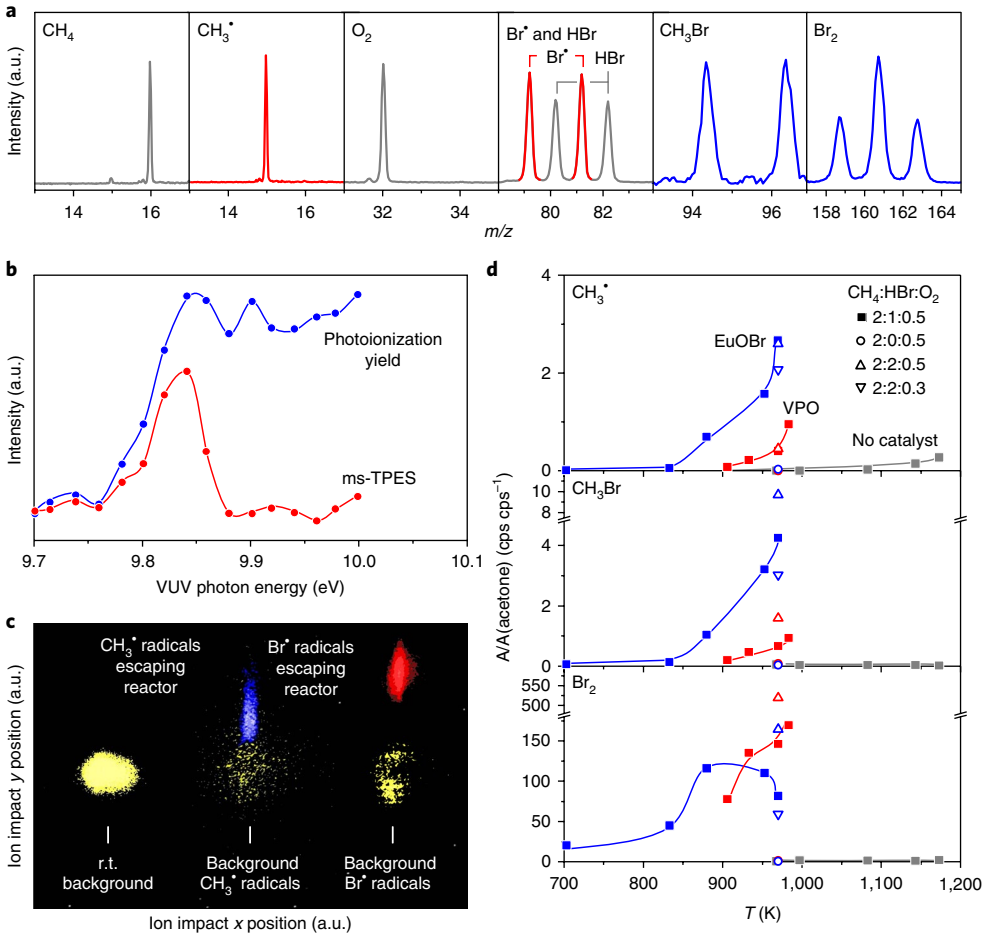

Fig. 3 | Radical detection in catalytic methane oxybromination. a, The representative mass spectra of different reactant (grey), product (blue) and intermediate radical (red) species detected in methane oxybromination over EuOBr (CH_4:HBr:O_2:Ar = 2:1:0.5, T = 970 K). **b**, The photoionization yield and photoion ms-TPES of the m/z = 15 ion. **c**, The velocity map images of the room temperature (r.t.) background (left); ions detected at m/z = 15 corresponding to methyl radicals (middle) and ions detected at m/z = 79/81 corresponding to bromine radicals (right) allows for the differentiation between methyl (blue) and bromine (red) radicals escaping directly from the reactor and the ones that are scattered or undergo momentum randomization upon multiple collisions with chamber walls (yellow) based on their position. **d**, The normalized peak areas of the signals corresponding to methyl radicals (top), methyl bromide (CH_3Br, middle) and bromine (Br_2, bottom) in methane oxybromination over VPO, EuOBr and in an empty reactor at different temperatures and concentrations of reactants (CH_4:HBr:O_2:Ar = 2:0–2:0.3–0.5:19–21). Peak areas of various species were normalized with respect to acetone as an internal standard present at a constant concentration in the chamber. All the tests were conducted using W_{cat} = 0.05 g and F_T = 23.5 cm^3.

background, Fig. 3c). Dissociative ionization would directly lead to a broadening of the velocity distribution perpendicular to the beam axis (x) due to the statistical release of excess energy as kinetic energy of the fragments. The CH_3^+ and Br^+ ions detected on oxybromination show a narrow distribution along the x axis and are thus formed by direct ionization of $CH_3^•$ and $Br^•$ present in the beam.

Besides the detection of $CH_3^•$ and $Br^•$ intermediates in methane oxybromination, PEPICO spectroscopy also enabled us to establish the relationships between their production and the formation of the reaction products (Fig. 3d, Supplementary Fig. 7). The onset of methane oxybromination in PEPICO spectroscopy experiments was approximately 150–200 K higher compared with the tests performed in the conventional reactor set-up. This can be rationalized by the significantly shorter residence time in the former tests (approximately 0.0004 s)[41] with respect to the fixed-bed reactor (~0.4 s), which necessitates higher temperatures to achieve the specific reaction rate that enables the detection of product formation, as also demonstrated by the experiments conducted at ambient pressure (Supplementary Fig. 8). A lower reactor pressure (~1–4 kPa compared to ~100 kPa) requires higher temperatures to achieve similar collision frequencies in the gas phase. While the internal energy distributions are broadened and shifted upwards, a difference of 150–200 K only results in a minor change to the reaction energy profile and the system does not fly over the potential energy surface. The validity of the conclusion made from PEPICO spectroscopy was further corroborated by the similar trends in product distribution observed from the steady-state experiments conducted at ambient pressure. At low temperatures, Br_2 was the only product (Fig. 3d), for which its evolution was accompanied by the formation of $Br^•$ (Supplementary Fig. 7). The onset of CH_3Br production was shifted to higher temperatures and was associated with the appearance of $CH_3^•$. Furthermore, the formation of this product was strongly correlated with the relative concentration of $CH_3^•$ and the ratio of the molar fractions of $CH_3^•$ and CH_3Br was estimated to be in the range of 0.5–1.5 on the basis of their reported ionization cross-sections[42,43]. These observations were additionally confirmed by conducting a control experiment under an identical feed composition in an empty reactor, which showed that the generation of $CH_3^•$ proceeds at temperatures approximately 200 K higher than the catalytic process (Fig. 3d, Supplementary Figs. 6,7). The concentration of $CH_3^•$ was much lower and $Br^•$ was hardly detectable. Notably, formation of CH_3Br could not be detected, which confirms

that the catalyst surface generates Br•, which initiates the formation of CH_3• and hence the production of CH_3Br. Further insights into the origin of CH_3• were obtained by varying the concentration of HBr and O_2 in the feed (Fig. 3d). In line with the positive reaction order with respect to HBr, a higher concentration of HBr enhanced the production of Br_2, Br• and CH_3Br, although the concentration of CH_3• remained almost unaltered. As exemplified for EuOBr, a decrease in O_2 content leads to a drop in production of CH_3Br, CH_3• and Br•. The removal of HBr from the feed completely halted the evolution of Br• and CH_3• and consequently the production of CH_3Br. Together with the strong correlation between CH_3• and CH_3Br formation, these results unequivocally demonstrate that the activation of CH_4 in the catalytic oxybromination involves gas-phase CH_3• generation through hydrogen abstraction from CH_4 by reactive Br•, the formation of which remains unresolved. Surface-catalysed oxidation of HBr and a propagation step of the gas-phase methane bromination might be potential sources.

Rationalization of the reaction pathway. DFT calculations were employed to gather a comprehensive molecular level picture of the interplay between the surface-catalysed HBr oxidation and methane bromination in the gas-phase using VPO as a model catalytic system (Fig. 4). The first step of HBr oxidation comprises dissociative O_2 adsorption, which is exothermic by −0.36 eV per oxygen atom adsorbed. In the next step, HBr is dissociatively adsorbed on VPO, yielding a surface bromine (Br*) and a proton, which binds to the neighbouring O*. This is an acid–base reaction and is therefore exothermic by −0.87 or −0.91 eV depending on the final position of the proton. The second molecule of HBr can then be adsorbed leaving a water molecule and the second Br* on the surface, which is exothermic by −0.42 eV. A desorption of the newly formed water molecule necessitates 1.31 eV that is partially compensated by entropic contributions. Notably, elimination of adsorbed Br* from the surface can proceed via two pathways. The first involves the recombination of Br* to generate Br_2 in the gas phase, the energy barrier of which is 0.60 eV. The second comprises desorption in the form of gas-phase radicals, Br•. This step can proceed after the adsorption of the first molecule of HBr and requires 1.30 eV. The formation of bromine radicals on EuOBr is less energy demanding, at 1.09 eV. Again, entropic contributions would render this desorption attainable at the reaction temperatures. These results reveal the importance of the surface-catalysed HBr oxidation in methane oxybromination, enabling the generation of both Br_2 and Br•, which are essential for CH_4 activation. Theory also predicts that these processes are barrierless at temperatures commonly used in oxybromination (approximately 753 K).

Once ejected from the catalyst surface, Br_2 and Br• are interrelated by the gas-phase equilibria in which the former might dissociate into the latter, and vice versa (Fig. 4)[21,23]. The calculations show that Br_2 dissociation is endothermic by 2.56 eV, which is higher than the experimentally determined value of 2.02 eV[23]. This energy barrier can be partially overcome at the temperatures at which oxybromination is conducted, enabling homolytic Br_2 splitting to occur to a certain degree. The bromine radicals produced by the catalyst surface or dissociation of Br_2 can abstract a hydrogen atom from CH_4, leading to the formation of CH_3• (Fig. 4). The computed energy barrier is 0.73 eV, and is comparable to the previously reported value of 0.78 eV[23]. However, if the gas-phase thermal and entropic contributions are taken into account, this step requires 1.25 eV (that is, 121 kJ mol^{-1}), which is comparable to the experimentally determined apparent activation energy of the catalytic methane oxybromination and non-catalytic methane bromination (Fig. 1c). The high energy barrier of the gas-phase CH_4 activation compared with

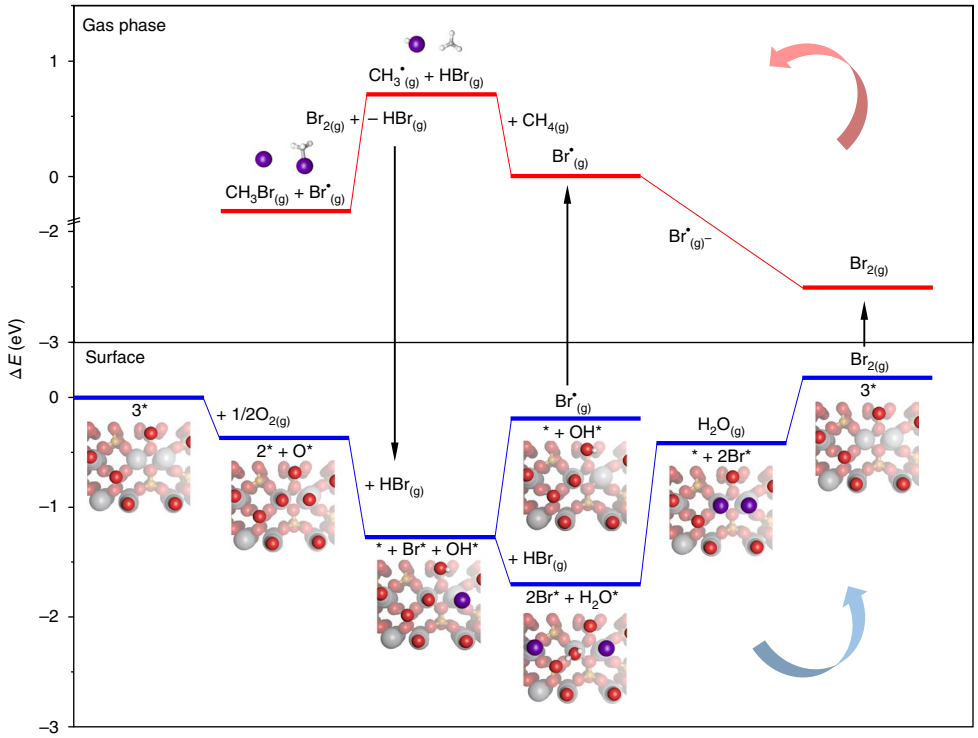

Fig. 4 | Reaction profile of catalytic methane oxybromination. The surface-catalysed reaction steps (blue, counterclockwise direction) that comprise the oxidation of HBr into Br• and molecular bromine (Br_2), and the gas-phase steps (red, counterclockwise direction) that comprise Br_2–Br• equilibrium, generation of CH_3• and formation of methyl bromide (CH_3Br) are interrelated by the desorption of Br• and Br_2, and regeneration of hydrogen bromide. Δ*E* denotes the energy difference with respect to the starting surface state and free reactants in the gas phase. O*, OH*, H_2O* and Br* denote the adsorbed oxygen, hydroxyl group, water molecule and bromine, respectively. *Free surface sites. Color codes: V, dark grey; P, orange; O, red; Br, purple; C, light grey; and H, white.

the barrierless evolution of Br• rationalizes the appearance of Br• at lower temperatures than CH_3• (Supplementary Fig. 6). It also implies that C–H scission is the rate-determining step of methane oxybromination, in good agreement with the reaction order of almost one with respect to CH_4. HBr produced in the previous step can regenerate Br• by surface oxidation, while CH_3• can enter a reaction with Br_2 forming CH_3Br and regenerating Br•. This step is reported to be exothermic by −1.08 eV and our calculations retrieve the same value[23]. The coupling of CH_3• into ethane (C_2H_6) is also exothermic (−4.10 eV, Supplementary Table 2), but kinetically much less favoured due to the substantially lower concentration of the short-lived radical intermediates compared with Br_2. This translates into a much higher frequency of CH_3•–Br_2 collisions, which explains the absence of C_2H_6 production in methane oxybromination. The formation of CH_2Br_2 primarily proceeds via CH_3Br reaction with Br• and Br_2, following a pathway analogous to that described for CH_4. The bromination of CH_3Br by second CH_3Br molecule (CH_3Br disproportionation) constitutes a negligible contribution, as shown experimentally in Supplementary Fig. 9.

The alternative reaction pathways, comprising CH_4 activation by: (1) an adsorbed oxygen (O*) and (2) an adsorbed bromine (Br*) on VPO have also been studied by DFT (Supplementary Table 2). Nonetheless, their energy barriers of 1.76 eV and 1.79 eV, respectively, exceed that for gas-phase methane bromination (1.25 eV), as well as the experimentally determined activation energy of methane oxybromination (Fig. 1c). The low propensity for CH_4 activation by surface O* is additionally corroborated by the substantially lower rates of methane oxidation compared with methane oxybromination (Fig. 1c). Similarly, the marginal contribution of surface C–H bond scission via Br* can be deduced from the extremely low surface bromine coverage, $\theta_{Br} < 0.01$, over VPO during methane oxybromination at ambient pressure, as determined by operando prompt gamma activation analysis (PGAA, Supplementary Fig. 10).

Conclusions

The detection of free Br• and CH_3• radicals by PEPICO spectroscopy complemented by kinetic analyses and DFT modelling confirmed that the catalytic oxybromination of methane involves the surface-catalysed HBr oxidation followed by the gas-phase CH_4 bromination. Accordingly, the catalyst surface evolves Br• and Br_2 to the gas phase, which are both barrierless processes under typical reaction conditions. This is in good agreement with the observation of Br_2 and Br• as the main product species at low reaction temperatures. In analogy with non-catalytic methane bromination, Br• induces the homolytic scission of C–H bonds in the gas-phase via hydrogen abstraction, yielding CH_3• and HBr, which can re-enter the oxidation step on the catalyst. The activation of CH_4 by Br• constitutes the rate-determining step in both the catalytic methane oxybromination and non-catalytic methane bromination, which is consistent with the substantial kinetics similarities between the two reactions, including a comparable operating temperature, product distribution, reaction order with respect to CH_4 and activation energy. The generated CH_3• can react with Br_2 producing CH_3Br and regenerating Br•, which can propagate the homolytic CH_4 activation in the previous step. The formation of CH_3Br through CH_3• is supported by the strong correlation between the molar fractions of these species. In the overall process, the catalytic surface plays an essential role as it enables a continuous recovery of Br• and Br_2 from HBr, suppressing the termination steps. These findings emphasize the importance of the radical chemistry in heterogeneously catalysed halogen-based processes for alkane activation and highlight the great potential of PEPICO spectroscopy to unravel complex reaction networks involving short-lived gaseous intermediates, which can be detected in an isotope-specific manner. Determining the contributions from the surface-catalysed and gas-phase reaction pathways has important practical implications for the prospective design of catalytic and reactor systems, as the latter have to provide the optimal balance between the desirable Br• and Br_2 evolution, their maximized interaction with CH_4 in the gas phase and minimized selectivity losses through the surface oxidation of bromomethanes and methane, thereby ensuring a high process efficiency.

Methods

Catalyst preparation and characterization. VPO and EuOBr were prepared according to methods described elsewhere[17]. Briefly, VPO was synthesized by refluxing a suspension of vanadium(V) oxide (V_2O_5, 15 g, Aldrich, ≥99.6%) in isobutanol (90 cm^3, Acros, >99%) and benzyl alcohol (60 cm^3, Sigma-Aldrich, >99%) for 3 h. After cooling down to room temperature, H_3PO_4 (Sigma-Aldrich, ≥85%) was added to achieve a molar P:V ratio of 1.2 and the mixture was then refluxed for another 16 h. The blue solid was recovered by filtration, then washed with isobutanol and methanol (Fluka, ≥99.9%). After drying under vacuum (5 kPa) at 373 K for 16 h, the material was heated in flowing N_2 (Pan Gas, purity 4.5) at 873 K for 5 h. EuOBr was prepared starting from europium(III) oxide (Eu_2O_3, 2 g, Sigma-Aldrich, 99.5%), which was calcined at 973 K for 5 h and then exposed to an HBr-containing gas mixture (HBr:O_2:He = 9:4.5:86.5, total flow rate $F_T = 100\ cm^3\ min^{-1}$) at 773 K for 5 h. Powder X-ray diffraction (XRD) was measured in a PANalytical X'Pert PRO-MPD diffractometer operated in Bragg–Brentano geometry using Ni-filtrated Cu Kα radiation ($\lambda = 1.54060$ Å). Data were recorded in 2θ range of 10–70° with an angular step size of 0.017° and counting time set to 0.026 s per step. N_2 isotherms at 77 K were measured in a Micromeritics TriStar analyser, after evacuation of the samples at 573 K and 5 kPa for 12 h. The Brunauer–Emmett–Teller (BET) method was applied to calculate the specific surface area.

Reaction tests. Methane oxybromination, methane oxidation, methane bromination and CH_3Br disproportionation experiments were performed in a continuous-flow reactor set-up (Supplementary Fig. 1). The gases CH_4 (PanGas, purity 5.0), HBr (Air Liquide, purity 2.8, anhydrous), CH_3Br (PanGas, 5 mol % in He 5.0), O_2 (PanGas, purity 5.0), Ar (PanGas, purity 5.0, used as internal standard) and He (PanGas, purity 5.0, used as carrier gas), were fed using a set of digital mass-flow controllers (Bronkhorst). Br_2 (ABCR, 99%) was fed using a syringe pump (Nexus 6000, Chemyx) with a water-cooled glass syringe (Hamilton, 1 cm^3) connected to a vaporizer operated at 343 K. In methane oxybromination, methane oxidation and CH_3Br disproportionation the catalyst (catalyst weight, $W_{cat} = 1$ g and particle size, $d_p = 0.4$-0.6 mm) was mixed with inert quartz particles (Thommen-Furler, $d_p = 0.2$–0.3 mm) and loaded in a quartz reactor (inner diameter, $d_r = 8$ mm) between the two plugs of quartz wool to form a fixed bed of constant volume ($V_{bed} = 2\ cm^3$). The post-catalyst zone was filled with quartz beads (Sigma-Aldrich, $d_p = 0.6$ mm) to minimize its volume. The influence of residence time on the CH_4 conversion in oxybromination was studied by using a reduced amount of catalyst ($W_{cat} = 0.012$–0.05 g) placed in the quartz reactor ($d_r = 4$ mm). The effect of the volume after the catalyst bed on the oxybromination performance was studied in quartz reactors with a catalyst zone of constant size ($W_{cat} = 0.07$ g, $d_p = 0.3$–0.4 mm, $d_r = 4$ mm) and different sizes of the post-catalyst zone. Non-catalytic gas-phase methane bromination was performed in an empty quartz reactor ($V_r = 2.5\ cm^3$). A K-type thermocouple fixed in a coaxial quartz thermowell with the tip positioned in the centre of the catalyst bed or void reactor in the case of bromination was used to monitor the temperature during the respective reactions. The reactor was placed in a home-made electric oven and heated in a He flow to the desired temperature ($T = 423$–873 K). It was allowed to stabilize for at least 30 min before the reaction mixture was admitted. The catalyst weights, F_T values and feed mixtures applied in the tests are compiled in Supplementary Table 1. Carbon-containing compounds (CH_4, CH_3Br, CH_2Br_2, CO and CO_2) and Ar were analysed online via a gas chromatograph equipped with a GS-Carbon PLOT column coupled to mass spectrometer (GC-MS, Agilent GC 6890, Agilent MSD 5973 N). Quantification of Br_2 was performed by its absorption in an impinging bottle filled with a 0.1 M KI solution ($Br_2 + 3I^- \rightarrow I_3^- + 2Br^-$) followed by iodometric titration (Mettler Toledo G20 Compact Titrator) of the formed triiodide ($I_3^- + {}_2S_2O_3^{2-} \rightarrow 3I^- + S_4O_6^{2-}$) with 0.01 M sodium thiosulfate solution (Aldrich, 99.99%). The effluent gas stream was finally passed through impinging bottles containing an aqueous NaOH solution (1 M) for neutralization.

The conversion of the reactant i, $X(i)$ (expressed as a percentage) and the reaction rate, $r_V(i)$, ($i = CH_4$ or CH_3Br, expressed in mol s^{-1} cm^{-3}) were calculated using equations (6) and (7), respectively,

$$X(i) = \frac{n(i)^{\text{inlet}} - n(i)^{\text{outlet}}}{n(i)^{\text{inlet}}} \times 100 \quad (6)$$

$$r_V(i) = \frac{n(i)^{\text{inlet}} - n(i)^{\text{outlet}}}{V} \quad (7)$$

where $n(i)^{\text{inlet}}$ and $n(i)^{\text{outlet}}$ are the respective molar flows of i at the reactor inlet and outlet, V corresponds to V_{bed} in the case of catalytic methane oxybromination and methane oxidation, and to V_r in the case of non-catalytic gas-phase methane bromination.

The selectivity to product *j*, *S*(*j*) and the yield of product *j*, *Y*(*j*) (both expressed as a percentage; where *j*: CH_3Br, CH_2Br_2, CO, CO_2) were calculated using equations (8) and (9), respectively,

$$S(j) = \frac{n(j)^{\text{outlet}}}{\sum^{\text{outlet}} n(j)^{\text{outlet}}} \times 100 \quad (8)$$

$$Y(j) = \frac{X(CH_4) \times S(j)}{100} \quad (9)$$

The yield of Br_2 was calculated according to equation (10),

$$Y(Br_2) = \frac{2 \times n(Br_2)^{\text{outlet}}}{n(HBr)^{\text{inlet}}} \times 100 \quad (10)$$

where $n(HBr)^{\text{inlet}}$ and $(Br_2)^{\text{outlet}}$ are the respective molar flows of HBr and Br_2 at the reactor inlet and outlet.

The error of the carbon mass balance, ε_C (expressed as a percentage), determined using equation (11),

$$\varepsilon_C = \frac{n(i)^{\text{inlet}} - \left(n(i)^{\text{outlet}} + \sum^{\text{outlet}} n(j)^{\text{outlet}}\right)}{n(i)^{\text{inlet}}} \times 100 \quad (11)$$

was less than 5% in all experiments. Each data point was calculated as an average of 2-4 measurements under given conditions.

Operando PEPICO spectroscopy. PEPICO spectroscopy experiments during methane oxybromination were performed using the PEPICO endstation at the VUV beamline of the Swiss Light Source (Fig. 2)[31,44,45]. The gases: CH_4, HBr, O_2 and Ar, were supplied by a set of digital mass-flow controllers to a tubular reactor ($d_r = 1$ mm) made of SiC placed in the source chamber. VPO and EuOBr ($W_{cat} = 0.05$ g) were deposited on the inner walls of the reactor by wash-coating using catalyst suspension in ethanol (Merck, absolute), followed by drying in air at 573 K for 1 h. An empty SiC reactor used in a control experiment was only washed with pure ethanol and dried using the same protocol. Two-ring electrodes connected to a d.c. power supply (Voltcraft) were applied to heat the reactor resistively, and its temperature was monitored by a type C thermocouple attached to the outside reactor wall at the mid point between the electrodes. The temperature of the flowing gas was calibrated against that measured at the outside wall and applied heating power in an independent experiment, which showed that these deviations are in the range of ±30 K. This calibration was used to recalculate the reaction temperature in the oxybromination experiments. The pressures at the reactor inlet and in the source chamber surrounding its outlet were 20 kPa and 2 mPa, respectively, and the effective pressure in the reaction zone was estimated to be in the range of 1–4 kPa based on the previous reports and by taking into account the flow rate, temperature and the reactor diameter applied in the experiments[41]. The central part of the molecular beam leaving the reactor was skimmed and fed into the analysis chamber, operating at 0.2 mPa. Synchrotron VUV radiation was used to ionize the sample; this was provided by a bending magnet, collimated by a mirror, dispersed by a 150 mm^{-1} grating working in grazing incidence and focused onto an exit slit in a rare gas filter by a second mirror. Higher grating orders in the 7–14 eV photon energy range are suppressed in the differentially pumped rare gas filter filled with 1 kPa of an Ar, Ne and Kr mixture over an optical length of 10 cm or by using an MgF_2 window. The photoions and photoelectrons are accelerated vertically in opposite directions by a constant field of 250 V cm^{-1} and the velocity map imaged onto two delay-line anode detectors (Roentdek, DLD40) in delayed coincidence[44]. The signal of the methyl radical ($CH_3^{\bullet}$) at $m/z = 15$ was recorded at a photon energy of 10 eV using an MgF_2 filter to suppress radiation above 10 eV quantitatively. The CH_3Br mass spectral peak was recorded at a photon energy of 10.6 eV. CH_4, O_2, HBr, Br_2 and bromine radicals ($Br^{\bullet}$) were detected by recording the fragmentation-free mass spectrum at a photon energy of 13 eV. The false coincidence background was subtracted in the time-of-flight mass spectra to obtain peak integrals. Photoion mass-selected threshold photoelectron spectra (ms-TPES) were obtained by subtracting the hot electron contribution using the procedure outlined in the literature[46]. The ratio of the molar fractions of $CH_3^{\bullet}$, $x(CH_3^{\bullet})$ and CH_3Br, $x(CH_3Br)$ was calculated according to equation (12):

$$\frac{x(CH_3)}{x(CH_3Br)} = \frac{\frac{A(CH_3)}{\sigma(CH_3)}}{\frac{A(CH_3Br)}{\sigma(CH_3Br)}} \quad (12)$$

where $A(CH_3^{\bullet})$ and $A(CH_3Br)$ are the respective integrated peak areas of $CH_3^{\bullet}$ and CH_3Br recorded using a photon energy of 10.6 eV, and $\sigma(CH_3^{\bullet})$ and $\sigma(CH_3Br)$ are the respective ionization cross-sections of $CH_3^{\bullet}$ and CH_3Br at this energy. The values of $\sigma(CH_3^{\bullet})$ of 6.3 Mb and $\sigma(CH_3Br)$ of 20.2 Mb at 10.6 eV were determined from the literature[42,43].

Computational details. The reaction profiles of both the heterogeneous and homogeneous reaction steps in the catalytic methane oxybromination were calculated by means of DFT using the Vienna ab initio simulation package (VASP) code[47,48] and the Perdew–Burcke–Ernzerhof functional, whereby the core electrons were represented by projector-augmented wave pseudopotentials and the valence electrons were expanded in plane waves with a cut-off energy of 450 eV[49,50]. VPO was taken as the representative compound for the simulations. The bulk was optimized with a dense *k*-point sampling and the cell parameters obtained were $a = 7.776$ Å, $b = 16.741$ Å and $c = 9.660$ Å. A cut along the lowest energy surface (100) was made to represent the active surface, where the terminal O atoms with dangling bonds were replaced by hydroxyl groups. The final stoichiometry of the slabs representing the surface is $V_{32}P_{32}O_{147}H_3$, which were interleaved by more than 15 Å. The reaction network was then studied on the uppermost part of the slab. The *k*-point sampling was set to 2 × 3 × 1. Test calculations were also performed on the EuOBr catalyst (PbFCl-type crystal structure, P4/nmm crystal symmetry)[51]. The surface was cut along the lowest energy [102] direction. The slab contained 7 layers and a (2 × 1) supercell was employed with at least 15 Å vacuum. High spin structures were computed for simplicity. The gas-phase reactions were run on a cubic box with a 15 Å side. The allocation of the transition states was performed using the climbing image nudged elastic band[52]. The nature of the transition states was confirmed by the identification of a single imaginary frequency in the diagonalization of the Hessian numerically computed by displacements of 0.015 Å. The reference bulk and surface structures of VPO and EuOBr have been uploaded to the ioChem-BD database[53,54].

Data availability. The data that support the plots within this paper and other findings of this study are available from the corresponding author upon reasonable request.

Received: 20 November 2017; Accepted: 6 April 2018;
Published online: 11 May 2018

References

1. Ito, T. & Lunsford, J. H. Synthesis of ethylene and ethane by partial oxidation of methane over lithium-doped magnesium oxide. *Nature* **314**, 721–722 (1985).
2. Bodke, A. S., Olschki, D. A., Schmidt, L. D. & Ranzi, E. High selectivities to ethylene by partial oxidation of ethane. *Science* **285**, 712–715 (1999).
3. Guo, X. et al. Direct, nonoxidative conversion of methane to ethylene, aromatics, and hydrogen. *Science* **344**, 616–619 (2014).
4. Gärtner, C. A., van Veen, A. C. & Lercher, J. A. Oxidative dehydrogenation of ethane: common principles and mechanistic aspects. *ChemCatChem* **5**, 3196–3217 (2013).
5. Sattler, J. J. H. B., Ruiz-Martinez, J., Santillan-Jimenez, E. & Weckhuysen, B. M. Catalytic dehydrogenation of light alkanes on metals and metal oxides. *Chem. Rev.* **114**, 10613–10653 (2014).
6. Kwapien, K. et al. Sites for methane activation on lithium-doped magnesium oxide surfaces. *Angew. Chem. Int. Ed.* **53**, 8774–8778 (2014).
7. Grundner, S. et al. Single-site trinuclear copper oxygen clusters in mordenite for selective conversion of methane to methanol. *Nat. Commun.* **6**, 7546 (2015).
8. Tomkins, P. et al. Isothermal cyclic conversion of methane into methanol over copper-exchanged zeolite at low temperature. *Angew. Chem. Int. Ed.* **55**, 5467–5471 (2016).
9. Latimer, A. A. et al. Understanding trends in C-H bond activation in heterogeneous catalysis. *Nat. Mater.* **16**, 225–229 (2016).
10. Gerceker, D. et al. Methane conversion to ethylene and aromatics on PtSn catalysts. *ACS Catal.* **7**, 2088–2100 (2017).
11. Driscoll, D. J., Martir, W., Wang, J. & Lunsford, J. H. Formation of gas-phase methyl radicals over MgO. *J. Am. Chem. Soc.* **107**, 58–63 (1985).
12. Luo, L. et al. Methyl radicals in oxidative coupling of methane directly confirmed by synchrotron VUV photoionization mass spectroscopy. *Sci. Rep.* **3**, 1625 (2013).
13. Hargreaves, J., Hutchings, G. & Joyner, R. Control of product selectivity in the partial oxidation of methane. *Nature* **348**, 428–429 (1990).
14. Horn, R. et al. Gas phase contributions to the catalytic formation of HCN from CH_4 and NH_3 over Pt: an in situ study by molecular beam mass spectrometry with threshold ionization. *Phys. Chem. Chem. Phys.* **6**, 4514–4521 (2004).
15. He, J. et al. Transformation of methane to propylene: a two-step reaction route catalyzed by modified CeO_2 nanocrystals and zeolites. *Angew. Chem. Int. Ed.* **51**, 2438–2442 (2012).
16. Paunović, V., Zichittella, G., Moser, M., Amrute, A. P. & Pérez-Ramírez, J. Catalyst design for natural-gas upgrading through oxybromination chemistry. *Nat. Chem.* **8**, 803–809 (2016).
17. Paunović, V. et al. Europium oxybromide catalysts for efficient bromine looping in natural gas valorization. *Angew. Chem. Int. Ed.* **56**, 9791–9795 (2017).
18. Ding, K. et al. Hydrodebromination and oligomerization of dibromomethane. *ACS Catal.* **2**, 479–486 (2012).
19. Lin, R., Amrute, A. P. & Pérez-Ramírez, J. Halogen-mediated conversion of hydrocarbons to commodities. *Chem. Rev.* **117**, 4182–4247 (2017).

20. Zichittella, G., Paunović, V., Amrute, A. P. & Pérez-Ramírez, J. Catalytic oxychlorination versus oxybromination for methane functionalization. *ACS Catal.* **7**, 1805–1817 (2017).
21. Kistiakowsky, G. B. & Van Artsdalen, E. R. Bromination of hydrocarbons. I. Photochemical and thermal bromination of methane and methyl bromine. Carbon-hydrogen bond strength in methane. *J. Chem. Phys.* **12**, 469–478 (1944).
22. Lorkovic, I. M. et al. Alkane bromination revisited: "reproportionation" in gas-phase methane bromination leads to higher selectivity for CH_3Br at moderate temperatures. *J. Phys. Chem. A* **110**, 8695–8700 (2006).
23. Ding, K., Metiu, H. & Stucky, G. D. The selective high-yield conversion of methane using iodine-catalyzed methane bromination. *ACS Catal.* **3**, 474–477 (2013).
24. Li, B. & Metiu, H. Does halogen adsorption activate the oxygen atom on an oxide surface? I. A study of Br_2 and HBr adsorption on La_2O_3 and La_2O_3 doped with Mg or Zr. *J. Phys. Chem. C.* **116**, 4137–4148 (2012).
25. Martir, W. & Lunsford, J. H. The formation of gas-phase π-allyl radicals from propylene over bismuth oxide and γ-bismuth molybdate catalysts. *J. Am. Chem. Soc.* **103**, 3728–3732 (1981).
26. Qi, F. Recent applications of synchrotron VUV photoionization mass spectrometry in combustion and energy research. *Acc. Chem. Res.* **10**, 68–78 (2010).
27. Li, Y. et al. Effect of the pressure on the catalytic oxidation of volatile organic compounds over Ag/Al_2O_3 catalyst. *Appl. Catal. B* **89**, 659–664 (2009).
28. Jiao, F. et al. Selective conversion of syngas to light olefins. *Science* **351**, 1065–1068 (2016).
29. Osborn, D. L. et al. Breaking through the false coincidence barrier in electron-ion coincidence experiments. *J. Chem. Phys.* **145**, 164202 (2016).
30. Tang, X., Garcia, G. A. & Nahon, L. CH_3^+ formation in the dissociation of energy-selected CH_3F^+ studied by double imaging electron/ion coincidences. *J. Phys. Chem. A* **119**, 5942–5950 (2015).
31. Sztáray, B. et al. CRF-PEPICO: double velocity map imaging photoelectron photoion coincidence spectroscopy for reaction kinetics studies. *J. Chem. Phys.* **147**, 13944 (2017).
32. Oßwald, P. et al. In situ flame chemistry tracing by imaging photoelectron photoion coincidence spectroscopy. *Rev. Sci. Instrum.* **85**, 025101 (2014).
33. Hemberger, P., Custodis, V. B. F., Bodi, A., Gerber, T. & van Bokhoven, J. A. Understanding the mechanism of catalytic fast pyrolysis by unveiling reactive intermediates in heterogeneous catalysis. *Nat. Commun.* **8**, 15946 (2017).
34. Eränen, K., Lindfors, L. E., Klingstedt, F. & Murzin, D. Y. Continuous reduction of NO with octane over a silver/alumina catalyst in oxygen-rich exhaust gases: combined heterogeneous and surface-mediated homogeneous reactions. *J. Catal.* **219**, 25–40 (2003).
35. Hemberger, P., Trevitt, A. J., Gerber, T., Ross, E. & Da Silva, G. Isomer-specific product detection of gas-phase xylyl radical rearrangement and decomposition using VUV synchrotron photoionization. *J. Phys. Chem. A* **118**, 3593–3604 (2014).
36. Lias, S. G. et al. in *NIST Chemistry WebBook: NIST Standard Reference Database* (National Institute of Standards and Technology, 2008).
37. Traeger, J. C. & McLoughlin, R. G. Absolute heats of formation for gas-phase cations. *J. Am. Chem. Soc.* **103**, 3647–3652 (1981).
38. Chang, Y.-C., Xiong, B., Bross, D. H., Ruscic, B. & Ng, C. Y. A vacuum ultraviolet laser pulsed field ionization-photoion study of methane (CH_4): determination of the appearance energy of methylium from methane with unprecedented precision and the resulting impact on the bond dissociation energies of CH_4 and CH_4^+. *Phys. Chem. Chem. Phys.* **19**, 9592–9605 (2017).
39. Kaposi, O., Riedel, M., Vass-Balthazar, K., Sanchez, G. R. & Lelik, L. Mass-spectrometric determination of thermochemical data of $CHBr_3$ and CBr_4 by study of their electron impact and heterogeneous pyrolytic decompositions. *Acta Chim. Acad. Sci. Hung.* **89**, 221 (1976).
40. DeCorpo, J. J., Bafus, D. A. & Franklin, J. L. Enthalpies of formation of the monohalomethyl radicals from mass spectrometric studies of the dihalomethanes. *J. Chem. Thermodyn.* **3**, 125–127 (1971).
41. Guan, Q. et al. The properties of a micro-reactor for the study of the unimolecular decomposition of large molecules. *Int. Rev. Phys. Chem.* **33**, 447–487 (2014).
42. Person, J. C. & Nicole, P. P. Isotope effects in the photoionization yields and in the absorption cross sections for methanol, ethanol, methyl bromide, and ethyl bromide. *J. Chem. Phys.* **55**, 3390–3397 (1971).
43. Gans, B. et al. Determination of the absolute photoionization cross sections of CH_3 and I produced from a pyrolysis source, by combined synchrotron and vacuum ultraviolet laser studies. *J. Phys. Chem. A* **114**, 3237–3246 (2010).
44. Bodi, A., Sztáray, B., Baer, T., Johnson, M. & Gerber, T. Data acquisition schemes for continuous two-particle time-of-flight coincidence experiments. *Rev. Sci. Instrum.* **78**, 084102 (2007).
45. Bodi, A. et al. Imaging photoelectron photoion coincidence spectroscopy with velocity focusing electron optics. *Rev. Sci. Instrum.* **80**, 034101 (2009).
46. Sztáray, B. & Baer, T. Suppression of hot electrons in threshold photoelectron photoion coincidence spectroscopy using velocity focusing optics. *Rev. Sci. Instrum.* **74**, 3763–3768 (2003).
47. Kresse, G. & Furthmüller, J. Efficiency of *ab-initio* total energy calculations for metals and semiconductors using a plane-wave basis set. *Comput. Mater. Sci.* **6**, 15–50 (1996).
48. Kresse, G. & Furthmüller, J. Efficient iterative schemes for *ab initio* total-energy calculations using a plane-wave basis set. *Phys. Rev. B* **54**, 11169–11186 (1996).
49. Perdew, J. P., Burke, K. & Ernzerhof, M. Generalized gradient approximation made simple. *Phys. Rev. Lett.* **77**, 3865–3868 (1996).
50. Blöchl, P. E. Projector augmented-wave method. *Phys. Rev. B* **50**, 17953–17979 (1994).
51. Mayer, I., Zolotov, S. & Kassierer, F. The crystal structure of rare earth and yttrium oxybromides. *Inorg. Chem.* **4**, 1637–1639 (1965).
52. Henkelman, G., Uberuaga, B. P. & Jónsson, H. Climbing image nudged elastic band method for finding saddle points and minimum energy paths. *J. Chem. Phys.* **113**, 9901–9904 (2000).
53. Álvarez-Moreno, M., de Graaf, C., López, N., Maseras, F., Poblet, J. M. & Bo, C. Managing the computational chemistry big data problem: the ioChem-BD platform. *J. Chem. Inf. Model.* **55**, 95–103 (2015).
54. López, N. *Computational Dataset for 'Evidence of Radical Chemistry in Catalytic Methane Oxybromination'* (*ioChem*, 2018); https://doi.org/10.19061/iochem-bd-1-71.

Acknowledgements

This work was supported by the Swiss National Science Foundation (project no. 200021-156107) and the Swiss Federal Office of Energy (contract no. SI/501269-01). D. Teschner from the Fritz Haber Institute of the Max Planck Society, Berlin; L. Szentmiklósi from the Centre for Energy Research, Hungarian Academy of Sciences, Budapest; and M. Moser are acknowledged for their help in performing prompt gamma activation analysis.

Author contributions

J.P.-R. conceived and coordinated all stages of this research. V.P. prepared and characterized the catalysts, and performed and analysed the steady-state tests. V.P., P.H. and A.B. conducted operando PEPICO spectroscopy experiments. P.H. and A.B. analysed the results of PEPICO spectroscopy. N.L. conducted the DFT calculations. The data were discussed among all the authors. V.P., P.H. and J.P.-R. wrote the paper with feedback from the other authors.

Competing interests

The authors declare that they have no competing interests.

Additional information